

Cite this: *RSC Adv.*, 2014, 4, 48236

Promotional effect of silver nanoparticles on the performance of N-doped TiO₂ photoanode-based dye-sensitized solar cells†

Su Pei Lim,^a Alagarsamy Pandikumar,^{*a} Nay Ming Huang,^{*a} Hong Ngee Lim,^{*bc} Guochen Gu^d and Ting Li Ma^d

We report the first successful application of an N-TiO₂-Ag nanocomposite as an efficient photoanode for highly efficient dye-sensitized solar cells (DSSC). The N-TiO₂-Ag nanocomposites with different Ag contents were prepared using a simple chemical reduction method and characterized using various suitable techniques. The DSSC assembled with the N-TiO₂-Ag-modified photoanode demonstrated an enhanced solar-to-electrical energy conversion efficiency of 8.15% compared to the photoanode of a DSSC composed of unmodified TiO₂ (2.19%) under full sunlight illumination (100 mW cm⁻², AM 1.5 G). This superior DSSC performance was due to the reduced band gap energy and retarded charge recombination that resulted from the introduction of plasmonic Ag nanoparticles on the surface of N-TiO₂. The influence of the Ag content on the overall efficiency was also investigated, and the optimum Ag content for N-TiO₂ was found to be 10 wt%. The enhanced solar energy conversion efficiency demonstrated by the N-TiO₂-Ag nanocomposite makes it a promising alternative to conventional photoanode-based DSSCs.

Received 4th September 2014
Accepted 22nd September 2014

DOI: 10.1039/c4ra09775k

www.rsc.org/advances

1. Introduction

Out of consideration for natural resource depletion and environmental issues, dye-sensitized solar cells (DSSCs) have emerged as promising candidates for harvesting solar power, because of their low cost, flexibility, ease of production, relatively high energy conversion efficiency, and low toxicity to the environment.¹ Encouragingly, significant progress has been achieved for DSSCs by introducing novel components such as electrolytes and dyes, along with various morphologies for the semiconductor materials. It is apparent that the further improvement of DSSCs is a key factor to accelerating their industrialization. Materials based on semiconductor oxides, especially titanium dioxide (TiO₂), have potential for DSSC applications. The major drawback associated with the use of TiO₂ is the random manner of its electron transport, which will

cause the electron-hole recombination process and hence affect the cell performance.^{2,3} In order to overcome this problem, designing a photoanode with an efficient transport pathway from the photoinjected charge carriers to the current collector seems to be a possible alternative to enhance the performance of DSSCs. With this aim, methods such as surface modification with metal, doping, semiconductor coupling, and hybridizing with carbon materials have been attempted.⁴⁻⁷

Nitrogen-doped TiO₂ possesses good photovoltaic properties. Hence, it has received much attention due to the narrowing of the band gap and shift to the visible region. The major limitation of the N-doping is the low concentration of N dopants that can be doped in the TiO₂ lattice, because the unstable N dopants in the TiO₂ lattice may escape to become N₂ or oxynitrides.⁸⁻¹⁰ Meanwhile, the photogenerated electrons tend to recombine at the mono-doping type of dopant sites, which is another limitation of N-doped TiO₂-based DSSCs.^{11,12} In order to overcome these limitations, N-doped TiO₂ has been modified with a noble metal such as Au,¹³ Ag,¹⁴ and Pt^{14,15} to prevent the recombination of the photogenerated electron-hole pairs and improve the charge transfer efficiency. In addition, studies have reported that the introduction of metal nanoparticles to the N-doped TiO₂ surface could enhance the amount of N that could be stabilized in TiO₂. The TiO₂-Ag nanocomposites have shown improved DSSC performances, since the Ag nanoparticles act as an electron sink for the photoinjected charge carriers and also show the plasmonic absorption effect, which maximizes the DSSC efficiency.¹⁶⁻¹⁸ The co-deposition of Ag on the N-doped

^aLow Dimensional Materials Research Centre, Department of Physics, Faculty of Science, University of Malaya, 50603 Kuala Lumpur, Malaysia. E-mail: pandikumarinbox@gmail.com; huangnayming@um.edu.my; janet_limhn@science.upm.edu.my

^bDepartment of Chemistry, Faculty of Science, Universiti Putra Malaysia, 43400 UPM Serdang, Selangor, Malaysia

^cFunctional Device Laboratory, Institute of Advanced Technology, Universiti Putra Malaysia, 43400 UPM Serdang, Selangor, Malaysia

^dGraduate School of Life Science and Systems Engineering, Kyushu Institute of Technology, 808 0196, Kitakyusyu, Japan

† Electronic supplementary information (ESI) available. See DOI: 10.1039/c4ra09775k

TiO₂ is more beneficial and has shown enhanced photocatalytic properties due to the synergistic effect that arises between the Ag and N-doped TiO₂.^{12,14}

Based on the above literature, so far the N-TiO₂ and TiO₂-Ag have been used separately as photoanodes in DSSCs. To the best of our knowledge, we explored the co-deposition of Ag nanoparticles on N-doped TiO₂ as a photoanode for a DSSC for the first time. We successfully developed a facile synthesis method to deposit Ag nanoparticles on N-TiO₂ using a simple chemical reduction method and characterized it using various analytical techniques. The DSSC assembled with the N-TiO₂-Ag-modified photoanode showed an enhanced conversion efficiency of 8.15% compared to the unmodified TiO₂ (2.19%). This enhanced efficiency due to the reduced band gap energy and retarded charge recombination resulted from the introduction of plasmonic Ag nanoparticles on the surface of N-TiO₂. The influence of the Ag content on the overall efficiency was also explored, and the optimum content was 10 wt%. This novel N-TiO₂-Ag nanocomposite could be a potential candidate for solar energy conversion.

2. Experimental methods

2.1. Materials

Titanium dioxide (P25) was purchased from Acros Organics. Silver nitrate (AgNO₃) and urea were received from Merck. Sodium borohydride (NaBH₄) was obtained from R&M chemicals. Indium tin oxide (ITO) conducting glass slides (7 Ω sq⁻¹) were purchased from Xin Yan Technology Limited, China. N719 (Ruthenizer 535-bisTBA) and Iodolyte Z-100 were received from Solaronix.

2.2. Material characterization techniques

The crystalline phases of the samples were determined *via* X-ray diffraction (XRD; D5000, Siemens), using copper Kα radiation ($\lambda = 1.5418 \text{ \AA}$) at a scan rate of $0.02^\circ \text{ s}^{-1}$. The morphology of each film was examined using field emission scanning electron microscopy (Hitachi, SU 8000), transmission electron microscopy (TEM) (Hitachi, HT-7700), and high resolution TEM (JEOL JEM-2100 F). The optical absorption properties in the spectral region of 190–900 nm were assessed using a Thermo Scientific Evolution 300 UV-vis spectrophotometer. Photoluminescence and Raman spectra were collected using a Renishaw inVia 2000 system with a laser emitting at 325 and 514 nm, respectively. X-ray photoelectron spectroscopy (XPS) measurements were performed using synchrotron radiation from beamline no. 3.2 at the Synchrotron Light Research Institute, Thailand.

2.3. Synthesis of N-TiO₂-Ag nanocomposite

The N-TiO₂-Ag nanocomposite was prepared using a chemical reduction method. Initially, N-TiO₂ was prepared by mixing P25 and urea (at a 1 : 1 weight ratio) and grounding it for at least 30 min in a mortar. It was then annealed in a furnace at 400 °C at a heating rate of $10^\circ \text{C min}^{-1}$ in air for 1 h. Subsequently, a pale yellow N-TiO₂ was obtained.¹³ After that, 500 mg of the pre-formed N-TiO₂ was added to an aqueous solution containing

AgNO₃. The amount of AgNO₃ used for the N-TiO₂ varied from 2.5 to 5, 10, and 20 wt%. The mixture was vigorously stirred for 30 min at room temperature. The reduction of Ag⁺ was carried out by the drop-wise addition of freshly prepared NaBH₄ until a change in the color of the solution was maintained. The yellowish-green appearance of the solution indicated the formation of the N-TiO₂-Ag nanocomposite, and the solution was continually stirred for another 30 min. The nanocomposite was collected and washed with distilled water and ethanol several times using centrifugation. Finally, the product was dried in an oven at 60 °C and stored in the dark.

2.4. Fabrication of N-TiO₂-Ag photoanode-modified DSSCs and evaluation of their performances

N-TiO₂-Ag-modified photoanodes were fabricated using the following procedure. Initially, 300 mg of the N-TiO₂-Ag nanocomposite was mixed in an ethanolic solution and stirred for 30 min. A 0.1 M quantity of TTIP was slowly introduced into the above reaction mixture and stirred until a homogenous solution was obtained. Finally, the N-TiO₂-Ag nanocomposite was coated on the conducting side of the ITO using the doctor-blade technique with the aid of scotch-3M tape and the thickness of the film was $\sim 12 \text{ }\mu\text{m}$. In order to obtain a stable photoanode, the film was dried at room temperature, sintered at 150 °C for 30 min in a muffle furnace, and then allowed to cool naturally to room temperature. The prepared N-TiO₂-Ag photoanodes were immersed in an ethanolic solution of 0.3 mM N719 (Ruthenizer 535-bisTBA) dye for 24 h at room temperature. The dye-adsorbed photoanode was withdrawn from the solution and immediately cleaned with ethanol. A platinum sputtered ITO was placed on a dye-adsorbed photoanode, and they were clamped firmly together. An electrolyte (Iodolyte Z-100, Solaronix) solution was introduced into the cell assembly by capillary action. An active area of 0.5 cm² was used to measure the cell performance. A 150 W Xenon arc lamp (Newport, Model 69907) containing a simulated AM 1.5 G filter with a manual shutter was used as a light source throughout the experiments. Prior to testing the photovoltaic parameter, an Avaspec-2048 fiber optic spectrophotometer was used to measure the light illumination intensity. Photocurrent signal measurements (*J*-*V* and *J*-*T* curves) were carried out with an active electrode area of 0.5 cm² using a computer-controlled VersaSTAT 3 Electrochemical Workstation (Princeton Applied Research, USA).

3. Results and discussion

3.1. Morphological studies of N-TiO₂-Ag nanocomposite

The microscopic morphologies of the as-prepared samples were studied using FESEM, TEM, and HRTEM. Fig. 1a shows the FESEM results for N-TiO₂, which appears to be spherical in shape with a uniform size. Upon the addition of Ag, no significant change in the morphology was observed for the film (Fig. 1b). The presence of Ag and N on the TiO₂ was confirmed by element mapping, as shown in Fig. 1c. The N-TiO₂-Ag thin film contained Ti, O, N, and Ag. Further, TEM images of the N-TiO₂-Ag were recorded and are shown in Fig. 1d. The TEM



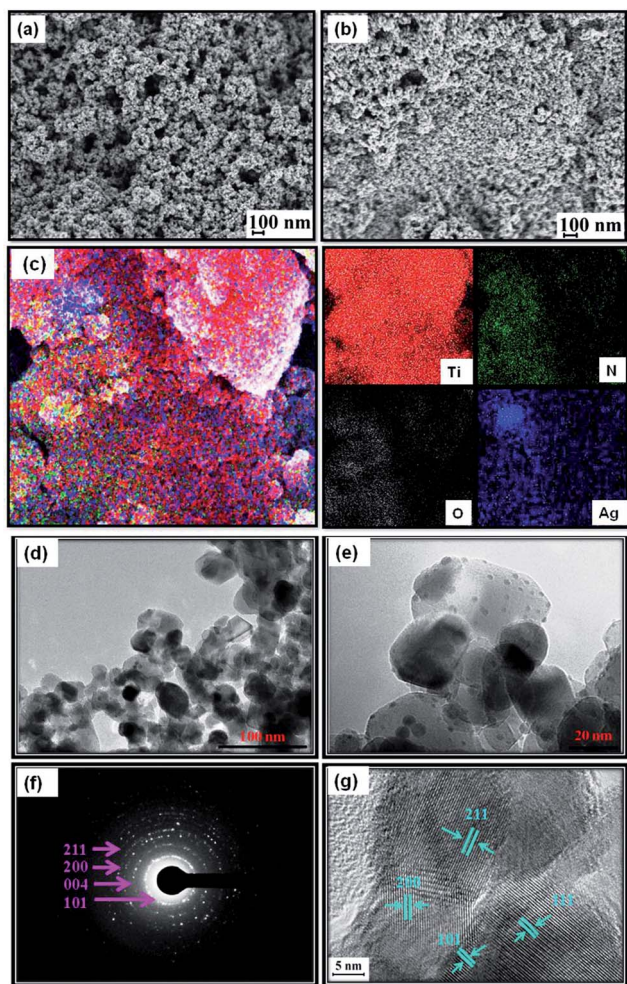


Fig. 1 FESEM images of (a) N-TiO₂ and (b) N-TiO₂-Ag (10 wt% Ag) (c) EDAX element mapping, (d and e) TEM images, (f) SAED pattern, and (g) lattice resolved TEM image of N-TiO₂-Ag.

images show that the N-TiO₂ nanoparticles are spherical in shape, with a particle size range of 20–25 nm. Fig. 1e clearly shows that the small spherical Ag nanoparticles with a particle size range of 2–4 nm are well distributed and decorated on the surface of the N-TiO₂. Fig. 1f depicted the selected area electron diffraction (SAED) pattern of the nanocrystalline particles. The pattern clearly reveals bright concentric rings, which are due to the diffraction from the (211), (111), (004), and (101) planes of the anatase TiO₂. The lattice resolved HRTEM image of the N-TiO₂-Ag (Fig. 1g) shows d-spacing values for the lattice fringes of 2.18 Å, 1.68 Å, 2.49 Å, and 1.89 Å, which correspond to the (111), (211), (101), and (200) planes of TiO₂.

3.2. XPS analysis of N-TiO₂-Ag nanocomposite

The XPS spectra of the TiO₂, N-TiO₂, and N-TiO₂-Ag were recorded to understand their chemical natures and are shown in Fig. 2. Fig. 2a shows the Ti 2p core-level spectra for the samples, in which two prominent peaks are observed at 454.1 and 459.9 eV corresponding to the binding energies of the Ti 2p_{3/2} and Ti 2p_{1/2} core levels due to the presence of the Ti(IV)

state. Fig. 2b shows the O 1s spectra of the TiO₂, N-TiO₂ and N-TiO₂-Ag, and the binding energy of the O 1s state of the samples is located at 530.9 eV, which is assigned to the bulk oxides (O²⁻) in the P25 lattice. The binding energy of the N 1s atom is observed at 399.5 eV (Fig. 2c). The binding energies found for the Ag 3d_{5/2} and Ag 3d_{3/2} levels are observed at 367.5 and 373.5 eV, respectively (Fig. 2d), with a peak separation of 6 eV due to the metallic silver.^{18,19} The XPS analysis results provide support for the existence of elements such as Ti, O, N, and Ag in the nanocomposite materials.

3.3. Crystalline nature of N-TiO₂-Ag nanocomposite

The XRD obtained pattern obtained for the N-TiO₂-Ag nanocomposite is shown in Fig. S1,† together with those for the TiO₂ and N-TiO₂. The TiO₂, N-TiO₂, and N-TiO₂-Ag films are composed of mixed anatase and rutile phases, which agrees with reference patterns JCPDS 83-2243 and 21-1276, respectively. The diffraction peaks at 25.3°, 38.8°, 48.35°, and 74.5° correspond to the anatase phase of TiO₂ and are assigned to the (101), (004), (200), and (215) crystallographic planes, respectively. In contrast, the peaks at 54.08° and 63.21° agree well with the rutile phase of TiO₂ and are assigned to the (220) and (002) crystallographic planes, respectively. The diffraction peaks related to the metallic Ag are located at 38.2°, 44.4°, and 64.6°, and they overlap each other. Thus, it is difficult to differentiate the Ag signals from the TiO₂ signals.

To further evaluate the phases in the prepared films, Raman studies were performed in the range of 100–1000 cm⁻¹, and the results are shown in Fig. 3a. The observed Raman peaks at 144, 199, 397, 516, and 635 cm⁻¹ are due to the anatase phase TiO₂. The rutile TiO₂ phase was observed at 445 cm⁻¹ (ref. 16, 20 and 21). This clearly indicates that the TiO₂ and N-TiO₂ nanoparticles contain a mixture of the anatase and rutile phases. The Raman signals of TiO₂ did not change after doping with nitrogen, which indicated that no phase transition occurred. However, no signals related to Ag particles were identified for the samples because of the relatively low concentration of Ag loaded onto the TiO₂ and its weak Raman scattering power. An interesting observation is that the peak intensities decreased with the deposition of Ag, although the position of the Raman signal remained the same but broadened. This indicates that there was an interaction between the Ag and TiO₂ that affected the Raman resonance of TiO₂.¹⁷ This observation shows that the deposition of Ag on TiO₂ and N-TiO₂ does not cause any phase transition, but may bring about an electronic environment change in the surroundings.^{13,20–22}

3.4. Optical properties of N-TiO₂-Ag nanocomposite

The UV-vis absorption spectra of the TiO₂, N-TiO₂, and N-TiO₂-Ag were recorded and are shown in Fig. S2a.† It can be seen that the prepared samples showed an intense absorption in the UV region. The bare TiO₂ could not absorb the visible light, and the absorption curve started to drop at 380 nm, which allowed the N-TiO₂ to absorb the visible light. This revealed that the prepared N-TiO₂ and N-TiO₂-Ag exhibited a wider and stronger absorption of visible light than the TiO₂. In addition, all of the



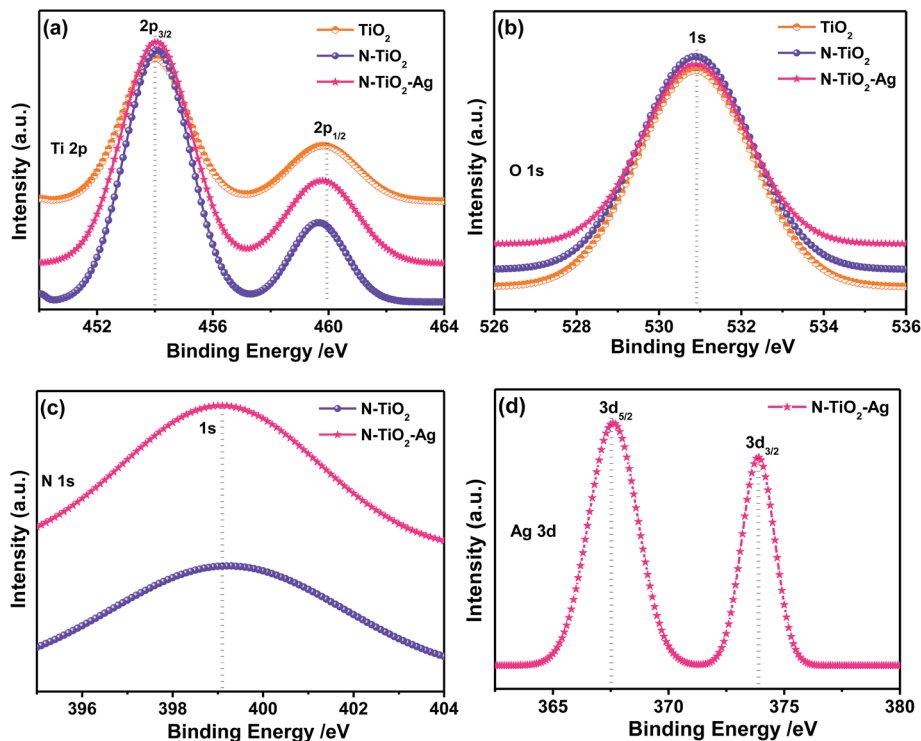


Fig. 2 XPS spectra of TiO_2 , N-TiO_2 , and $\text{N-TiO}_2\text{-Ag}$ (10 wt% Ag) and their corresponding (a) Ti 2p (b) O 1s (c) N 1s, and (d) Ag 3d core-level spectra.

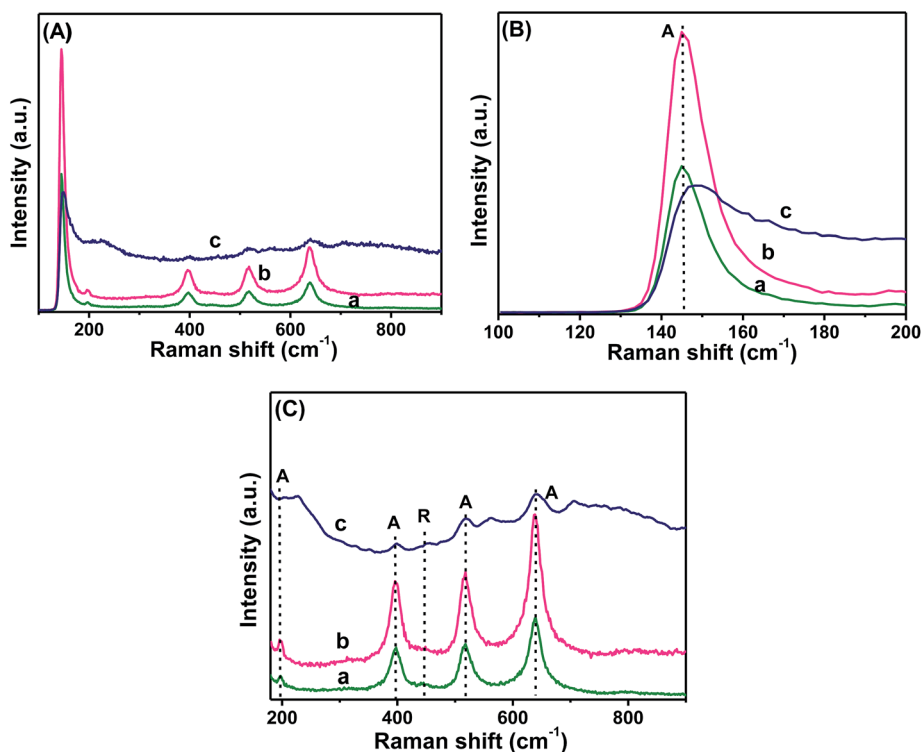


Fig. 3 Raman spectra of (a) TiO_2 , (b) N-TiO_2 , and (c) $\text{N-TiO}_2\text{-Ag}$ (10 wt% Ag) in different frequency regions: (A) 100–900 cm^{-1} , (B) 100–200 cm^{-1} , and (C) 180–900 cm^{-1} , which are provided separately for better clarity of the anatase and rutile phase TiO_2 .



N-TiO₂-Ag exhibited a significant absorption of both ultraviolet and visible light, along with an absorption band observed at ~500 nm due to the Ag nanoparticles' characteristic surface plasmon resonance (SPR) band. The SPR effect of the Ag nanoparticles could extend the light absorption to longer wavelengths, increasing the light scattering and motivating photogenerated carriers in the semiconductor by transferring the plasmonic energy from the Ag to the N-TiO₂ and N-TiO₂ semiconductor.²³ Upon the deposition of Ag on the TiO₂ and N-TiO₂ surfaces, the Schottky barrier was formed between the Ag and the TiO₂ and N-TiO₂, which acted as an electron sink, thus enhancing the separation of electron-hole pairs.²⁴ Further, it was found that simultaneously doping TiO₂ with N and modifying it with Ag made its band gap narrow, which is beneficial for improving the solar energy conversion efficiency. The band-gap energies (E_{bg}) of the TiO₂, N-TiO₂, and N-TiO₂-Ag were calculated using the well-known Tauc's plot method (Fig. S2(b-d)†).¹⁶ The calculated E_{bg} values for TiO₂, N-TiO₂, and N-TiO₂-Ag were 3.31, 3.23, and 3.04 eV, respectively. A remarkable reduction in the E_{bg} value for N-TiO₂ was observed due to the substitution of oxygen by nitrogen in the TiO₂ lattice. Mixing the N 2p states with the O 2p states resulted in a narrowing of the E_{bg} of TiO₂. When Ag nanoparticles were added to N-TiO₂, the E_{bg} was further decreased. This was because the free electron properties were exhibited with a downward shift in the conduction band and an upward shift in the valence band, which led to a decrease in the band-gap value.

UV-vis absorption spectra for N719 dye adsorbed TiO₂ and N-TiO₂ photoanodes were recorded and shown in Fig. S3a.† After coated with N719 dye, both TiO₂ and N-TiO₂ photoanodes showed a significant absorption in the region of 510–520 nm. The TiO₂ and N-TiO₂ show a maximum absorption at 507 nm and 520 nm, respectively. Addition of N into TiO₂ enhances the absorption in the region of 400–700 nm than that the bare TiO₂/N719 photoanode and it showed a red shift in the maximum absorption. Large amount of incident light is being absorbed in the broader wavelength range of 400–700 nm for N-TiO₂ photoanode as compared to 400–600 nm with TiO₂ photoanode. Higher portion of incident light absorption in the visible region by N-TiO₂ photoanode, suggests that this photoanode would efficiently harvest the sunlight especially in the visible region if used in DSSC. Furthermore, the band gap energy (E_{bg}) of the TiO₂ and N-TiO₂ photoanode is also determined (Fig. S3b and c†). It is observed that E_{bg} value is slightly decreased from 3.31 to 3.23 eV upon doping of N. Hence, we can conclude that the incorporating of N successfully reduced the band-gap and helped to extent the light absorption in the visible region.

Understanding the charge recombination process for a semiconductor is crucial because it would significantly influence the photoelectrochemical properties and DSSC performance. The TiO₂ absorbs incident photons with sufficient energy equal to or higher than the band-gap energy, and it produces photoinduced charge carriers ($h^+ \dots e^-$). The recombination of photoinduced electrons and holes releases energy in the form of photoluminescence. Hence, a lower PL intensity indicates less charge recombination. The observed PL spectra for the TiO₂, N-TiO₂, and N-TiO₂-Ag are shown in Fig. 4a. A

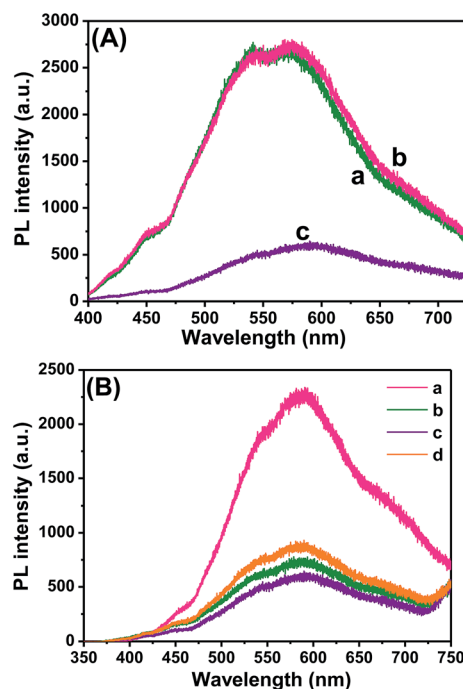


Fig. 4 (A) Photoluminescence spectra of (A) TiO₂, (b) N-TiO₂, and (c) N-TiO₂-Ag (10 wt% Ag). (B) N-TiO₂-Ag nanocomposite thin films with (a) 2.5, (b) 5, (c) 10, and (d) 20 wt% of Ag content.

broad peak with a maximum emission at around 580 nm can be observed for the TiO₂, N-TiO₂, and N-TiO₂-Ag. The TiO₂ and N-TiO₂ showed higher PL intensities due to the rapid recombination of photoinduced charge carriers. The PL intensity decreased when Ag was introduced to the N-TiO₂. This is mainly attributed to the formation of a Schottky barrier at the Ag and N-TiO₂ interface, which could act as an electron sink to efficiently prevent the electron-hole recombination process.²⁵ N-TiO₂-Ag with 10% Ag showed the lowest PL emission intensity, which indicated the least electron-hole recombination compared to 2.5, 5, and 20% Ag content on the TiO₂ surface, as seen in Fig. 4b.

3.5. Photovoltaic performances of N-TiO₂-Ag-modified photoanode-based DSSCs

The photovoltaic performances of the TiO₂, N-TiO₂, and N-TiO₂-Ag photoanode-based DSSCs were investigated under simulated solar AM 1.5 G irradiation, and the results are shown in Fig. 5. The parameters are summarized in Table 1. The photocurrent density–photovoltage (J - V) curve of the N-TiO₂-Ag photoanode-based DSSC shows a very high short-circuit current density of up to 21.51 mA cm⁻². The N-TiO₂-Ag photoanode showed an enhanced solar energy conversion (η) of 8.15%, which was higher than those of the TiO₂-Ag (4.86%), N-TiO₂ (2.93%), and pure TiO₂ (2.19%) photoanode-based DSSCs. The Ag nanoparticles showed a promotional effect on the overall energy conversion due to the surface plasmon resonance and synergetic effect between the Ag and N-TiO₂. The presence of N could extend the absorption of TiO₂ into the visible region.



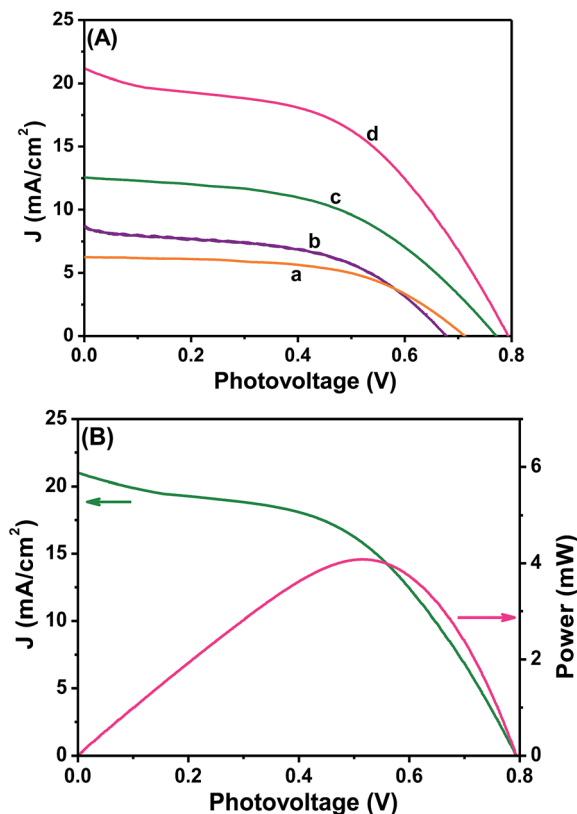


Fig. 5 (A) Photocurrent density–photovoltage curves obtained for (a) TiO_2 , (b) N-TiO_2 , and (c) $\text{N-TiO}_2\text{-Ag}$ (10 wt% Ag) photoanode-modified DSSCs. (B) Power output–photovoltage curves obtained for $\text{N-TiO}_2\text{-Ag}$ (10 wt% Ag) photoanode-modified DSSC.

Table 1 Photovoltaic parameters of various photoanode based DSSCs^a

Photoanode	J_{sc} (mA cm^{-2})	V_{oc} (V)	J_{max} (mA cm^{-2})	V_{max} (V)	FF	η (%)
TiO_2	6.27	0.70	5.25	0.49	0.59	2.57
N-TiO_2	8.77	0.68	6.10	0.48	0.49	2.93
$\text{TiO}_2\text{-Ag}$	12.19	0.77	9.34	0.52	0.52	4.86
$\text{N-TiO}_2\text{-Ag}$	21.51	0.79	15.99	0.51	0.48	8.15

^a The DSSC performance was evaluated under 100 mW cm^{-2} of simulated AM 1.5 G solar light irradiation. J_{sc} : short-circuit current density; V_{oc} : open-circuit voltage; J_{max} : Maximum photocurrent density; V_{max} : maximum photovoltage; FF: fill factor; η : power conversion efficiency. Area of the cell electrode was 0.5 cm^2 .

Moreover, the deposition of Ag onto the N-TiO_2 resulted in a change in the Fermi energy level. The electrons in the conduction band of the TiO_2 could be effectively captured by the Ag until the Fermi level equilibrium was obtained, which minimized the charge recombination process and thus improved the DSSC performance.

In order to achieve a higher performance for the DSSC, it is very important to optimize the Ag content in the photoanode. In this regard, the loading of the Ag content in the photoanode was varied to enhance the DSSC performance. Photocurrent

density–photovoltage voltage (J – V) curves were recorded for the $\text{N-TiO}_2\text{-Ag}$ nanocomposite-modified photoanodes with different Ag contents and are shown in Fig. 6. Their corresponding photovoltaic parameters are given in Table 2. The obtained conversion efficiencies for pristine N-TiO_2 and N-TiO_2 with 10 wt% Ag were 2.93% and 8.15%, respectively. In contrast, for 2.5, 5, and 20 wt% of Ag, the conversion efficiencies were 2.47%, 7.44%, and 1.63%, respectively. The observed results clearly revealed that the conversion efficiency of a DSSC was increased with an increase in the Ag content in the photoanode until it reached a maximum of 10 wt%. A further increase in the Ag content eventually led to a decrease in the conversion efficiency (Fig. 6a and Table 2). This decrease in the efficiency at a high Ag loading could be attributed to the following reasons: (i) the absorption and scattering of incident photons,^{26,27} (ii) the shielding of the TiO_2 /electrolyte interface from irradiation,²⁸ and (iii) the excess Ag may have undergone photooxidation by the photogenerated holes and/or surface hydroxyl radicals present in the TiO_2 particles.²⁹ Consequently, the overall conversion efficiency of the DSSC deteriorated. The J_{sc} was increased with the increasing Ag content and attained a maximum of 22.51 mA cm^{-2} at a loading of 5% (Fig. S4†). Further, J_{sc} decreased to 20.18 mA cm^{-2} with 20% Ag loading in

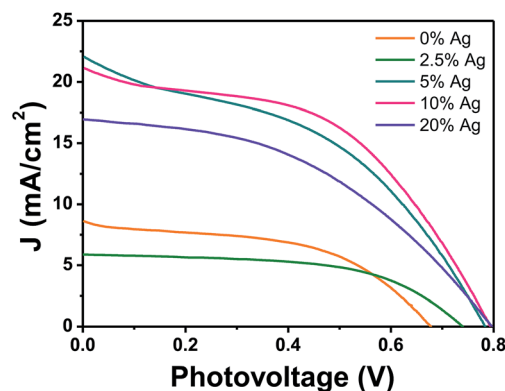


Fig. 6 Photocurrent density–photovoltage (J – V) curves obtained for $\text{N-TiO}_2\text{-Ag}$ nanocomposite photoanode-modified DSSCs with different Ag contents.

Table 2 Photovoltaic parameters of fabricated $\text{N-TiO}_2\text{-Ag}$ photoanode based DSSCs^a

Ag (%)	J_{sc} (mA cm^{-2})	V_{oc} (V)	J_{max} (mA cm^{-2})	V_{max} (V)	FF	η (%)
0	8.77	0.68	6.10	0.48	0.49	2.93
2.5	5.90	0.74	4.66	0.53	0.57	2.47
5	22.51	0.78	14.87	0.50	0.42	7.44
10	21.51	0.79	15.99	0.51	0.48	8.15
20	20.18	0.80	12.45	0.58	0.37	5.98

^a The DSSC performance was evaluated under 100 mW cm^{-2} of simulated AM 1.5 G solar light irradiation. J_{sc} : short-circuit current density; V_{oc} : open-circuit voltage; J_{max} : maximum photocurrent density; V_{max} : maximum photovoltage; FF: fill factor; η : power conversion efficiency. Area of the cell electrode was 0.5 cm^2 .

the photoanode of the DSSC. It can also be seen that the V_{oc} trends were almost the same, within the range of ~ 0.68 – 0.80 V. The J_{max} and V_{max} values of the device also followed trends similar to J_{sc} and V_{oc} (Fig. S4†).

The stability of N-TiO₂-Ag photoanode based DSSC was also studied under the light illumination “on-off” condition (Fig. S5†). The observed photocurrent density–time (J - T) profile is in agreement with its J - V characteristics. As soon as the light is turned ‘on’, the photocurrent spike to a maximum value and showed steady-state current as well. When the light is turned ‘off’, there is sudden fall in the photocurrent and no current in the dark condition. The steady-state of the maximum photocurrent remains the same after several ‘on-off’ cycles which revealed that the cells show good stability.

3.6. Electrochemical behavior of N-TiO₂-Ag-modified photoanode

In order to obtain deep insights into the interfacial charge transfer process within the fabricated DSSC, the electrochemical impedance spectra (EIS) were recorded in the frequency range of 0.01 Hz to 100 KHz and are shown in Fig. 7. A well-defined semicircle in the middle frequency region can be observed for the N-TiO₂-Ag nanocomposite-modified photoanode-based DSSC. The intersection of the high frequency semicircle at the real axis represents the equivalent series resistance of the device (R_s). The arc in the middle frequency range between 1 and 1000 Hz represents the charge transfer resistance (R_{ct}) between the dye-adsorbed photoanode and the electrolyte interface.^{2,30} Fig. 7A shows the Nyquist plot of

N-TiO₂ with different contents of Ag. Here, the R_s value can be ignored since it remains fairly consistent ($15\ \Omega$), and the DSSC components are the same, except for the different concentrations of Ag in the photoanode. The changes in R_{ct} can mainly be attributed to the changes in the Ag content in the photoanode, which contributed the most to the internal impedance. An increase in the R_{ct} value of the N-TiO₂-Ag-based photoanode was observed with the increasing Ag content. Thus, a photoanode that contained less Ag had a lower R_{ct} value, which corresponded to the efficient electron transfer process between the photoanode and electrolyte interface. The Nyquist plot of the different photoanodes is shown in Fig. 7B. As demonstrated by the Nyquist plot, both the real (Z') and imaginary (Z'') parts of the total impedance, as well as R_{ct} , increased in the order TiO₂ < N-TiO₂ < N-TiO₂-Ag, which showed the crucial dependence of the N and Ag incorporation on the charge transport. The increase in the R_{ct} value is more beneficial to suppress the charge recombination and could influence the short circuit current (J_{sc}) of the DSSC. The R_s value also decreases with the addition of N and Ag. Therefore, the origin of the higher J_{sc} in N-TiO₂-Ag is expected to arise from the R_s , R_{ct} , and charge transport dynamics determined by the electron lifetime (τ_n). From the Bode phase plots (Fig. 7C and D), the frequency was apparently shifted to the lower frequency region with the addition of N and Ag. The maximum frequencies (ω_{max}) in the middle frequency region of the Bode plots of TiO₂ and N-TiO₂-Ag were 3162.27 Hz and 1995.26 Hz, respectively. Since ω_{max} is inversely associated with the electron lifetime, $\tau_n = 1/(2\pi f)$,^{31,32} a decrease in ω_{max} indicates a reduced rate for

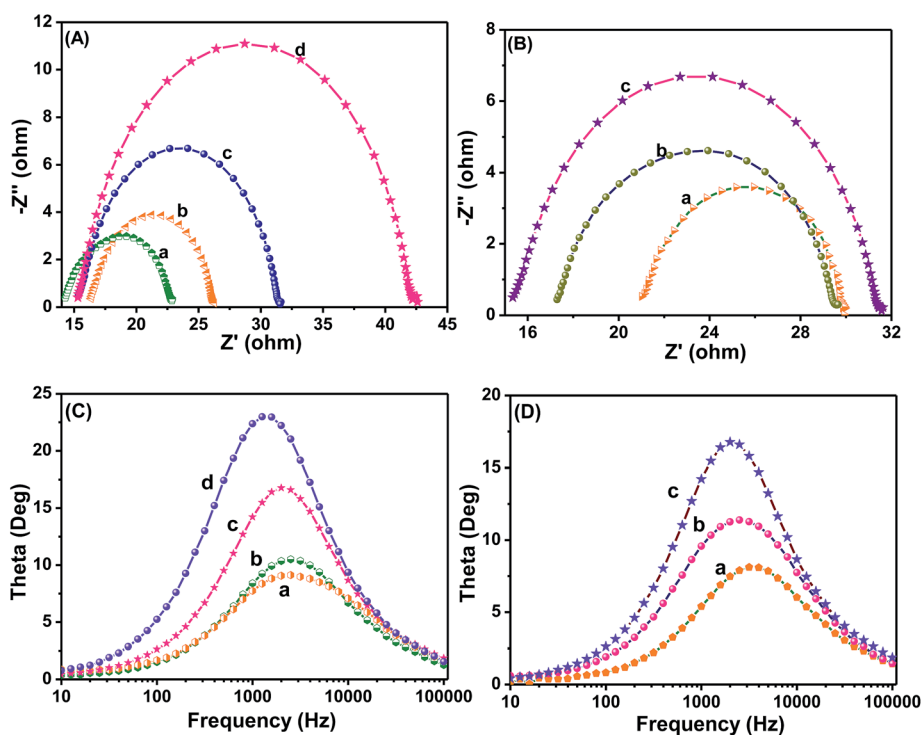


Fig. 7 (A) Nyquist plot and (C) Bode phase plots obtained for N-TiO₂-Ag nanocomposite-modified photoanodes with (a) 2.5, (b) 5, (c) 10, and (d) 20 wt% of Ag content. (B) Nyquist plot and (D) Bode phase plots of (a) TiO₂, (b) N-TiO₂, and (c) N-TiO₂-Ag (10 wt% Ag).



Table 3 EIS analysis results for fabricated DSSC^a

Photoanode	R_s (Ω)	R_{ct} (Ω)	C_μ (μ F)	τ_s (ms)	τ_n (ms)	η_c (%)
TiO ₂	21.01	8.91	7.10	0.14	0.06	29
N-TiO ₂	17.21	12.36	8.12	0.13	0.10	41
N-TiO ₂ -Ag	15.34	20.28	6.23	0.09	0.12	57

^a The electrochemical impedance spectra (EIS) were recorded at an applied bias of -0.7 V in the frequency range of 0.01 Hz to 100 KHz. R_s : device resistance; R_{ct} : charge transfer resistance; C_μ : chemical capacitance; τ_s : electron transport time; τ_n : electron lifetime; η_c : charge collection efficiency.

the charge-recombination process in a DSSC. Electrons with longer τ_n will survive recombination, as characterized by a larger R_{ct} .

Furthermore, Table 3 and Fig. S6† summarizes the results of the Nyquist plot. The N-TiO₂-Ag exhibited a faster electron transport time ($\tau_s = R_s \times C_\mu$)^{31,33,34} than TiO₂ and N-TiO₂. Hence, its electron lifetime ($\tau_n = R_{ct} \times C_\mu$)^{31,33,34} was significantly increased, and electrons survived the recombination. The photovoltaic performance of a DSSC is clearly reflected by the charge collection efficiency (η_c) derived from $\eta_c = (1 + R_s/R_{ct})^{-1}$.^{31,33,35} Eventually, the charge collection efficiency was significantly increased with the addition of N and Ag. We can conclude that, as a result of the longer τ_n and larger R_{ct} , the devices fabricated using N-TiO₂-Ag showed improved J_{sc} values compared to TiO₂ and N-TiO₂.

3.7. Operation principle of N-TiO₂-Ag-modified photoanode-based DSSC

The operation principle of the DSSC based on the N-TiO₂-Ag-modified photoelectrode under illumination is shown in Fig. 8a. The DSSC is based on the photo-excitation of the dye, followed by electron injection into the conduction band of the TiO₂ nanoparticle. During light irradiation, the dye absorbs incident light and promotes electrons to the excited state. The excited electrons are injected into Ag nanoparticles and then transferred to the conduction bands of TiO₂ nanoparticles. The dye is then oxidized by receiving electrons from the electrolyte through the redox system, and is ready to be used again. The electrolyte itself will be regenerated *via* the platinum counter electrode, by electrons passing through the external circuit. In our study, the Ag deposited onto the N-TiO₂ not only acted as an electron sink for an efficient charge transfer but could also be used as a scattering element for plasmonic scattering to trap the light and near-field coupled with the dye molecules.³⁶ This will eventually improve the optical absorption of dye, resulting in a significant photocurrent enhancement (Fig. 8b). Additionally, the incorporation of Ag also resulted in a change in the Fermi energy level. A large number of electrons accumulated on the surfaces of Ag nanoparticles due to the surface plasmon resonance effect. The accumulation of electrons on Ag nanoparticles shifted the position of the Fermi level closer to the conduction band of TiO₂.³⁷ The excited electrons in the Ag nanoparticles transferred to the conduction band of TiO₂ and were collected

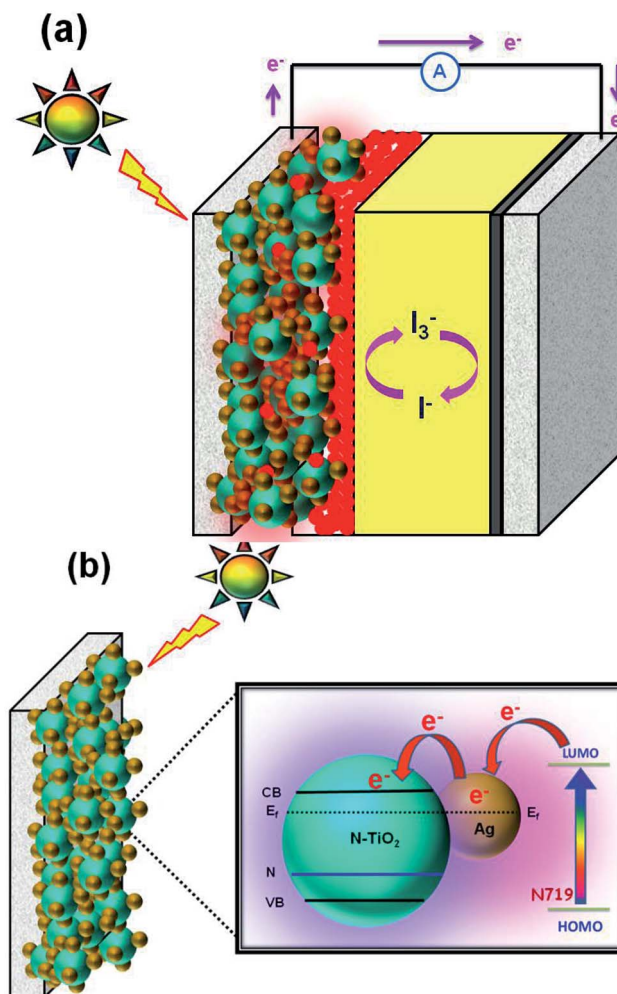


Fig. 8 (a) Schematic diagram and (b) charge transfer mechanism for N-TiO₂-Ag photoanode-modified DSSC.

by the current collector (ITO). Thus, the photocurrent was improved under irradiation in the visible region.³⁸ In this way, the photovoltaic performance significantly improved with the enhancement of absorption in the visible region due to the surface plasmon resonance of the Ag nanoparticles. In addition to the ideal property of Ag nanoparticles, the presence of the N also successfully reduced the band-gap and helped to shift the optical absorbance toward the visible region. The incorporation of N in TiO₂ that existed in the form of N-Ti-O would partially convert the system from Ti⁴⁺ to Ti³⁺ and effectively contributed toward visible light absorption.^{39,40}

4. Conclusion

In summary, a facile route to prepare Ag nanoparticles deposited on N-TiO₂ *via* a simple chemical reduction method was demonstrated in this report. The DSSC fabricated with N-TiO₂-Ag showed an enhanced solar-to-electrical energy conversion efficiency of 8.15% compared to the photoanode of a DSSC composed of unmodified TiO₂ (2.19%) under simulated solar irradiation of 100 mW cm⁻² with AM 1.5 G. The improvement was mainly



attributed to the Ag nanoparticles, which enhanced the visible light adsorption due to a light harvesting property in the visible range as a result of the surface plasmon resonance effect. In addition, the promotion of the interfacial charge transfer effectively minimized the charge recombination process. The optimum Ag content in the N-TiO₂-Ag for an efficient photoanode was found to be 10 wt%. In addition, the presence of N was also successfully reduced the band gap and helped to shift the optical absorbance toward the visible region. The conversion efficiency was nearly threefold that of unmodified TiO₂. The synergetic effects of the Ag nanoparticles, surface plasmon resonance effect, reduction in the band gap, and effective charge transfer ameliorated the photocurrent generation and conversion efficiency of DSSCs.

Conflict of interest

The author(s) declare(s) that there is no conflict of interest regarding the publication of this article.

Acknowledgements

This work was financially supported by a University of Malaya Research Grant Program (RP007C/13AFR), the Science Fund from the Ministry of Science, Technology and Innovation (06-01-04-SF1513), a High Impact Research Grant from the Ministry of Higher Education of Malaysia (UM.C/625/1/HIR/MOHE/SC/21), and a University of Malaya Postgraduate Research Grant (PG107-2012B).

References

- 1 B. O'Regan and M. Gratzel, *Nature*, 1991, **353**, 737–740.
- 2 J. van de Lagemaat, N. G. Park and A. J. Frank, *J. Phys. Chem. B*, 2000, **104**, 2044–2052.
- 3 N. Kopidakis, N. R. Neale, K. Zhu, J. van de Lagemaat and A. J. Frank, *Appl. Phys. Lett.*, 2005, **87**, 202106.
- 4 Y. Lai, H. Zhuang, K. Xie, D. Gong, Y. Tang, C. L. L. Sun and Z. Chen, *New J. Chem.*, 2010, 1335–1340.
- 5 J. M. Macak, F. Schmidt-Stein and P. Schmuki, *Electrochem. Commun.*, 2007, **9**, 1783–1787.
- 6 L. Yang, D. He, Q. Cai and C. A. Grimes, *J. Phys. Chem. C*, 2007, **111**, 8214–8217.
- 7 H. Zhao, Y. Chen, X. Quan and X. Ruan, *Chin. Sci. Bull.*, 2007, **52**, 1456–1461.
- 8 M. Batzill, E. H. Morales and U. Diebold, *Phys. Rev. Lett.*, 2006, **96**, 026103.
- 9 A. Nambu, J. Graciani, J. A. Rodriguez, Q. Wu, E. Fujita and J. Fdez Sanz, *J. Phys. Chem.*, 2006, **125**, 094706.
- 10 J. Graciani, L. J. Álvarez, J. A. Rodriguez and J. F. Sanz, *J. Phys. Chem. C*, 2008, **112**, 2624–2631.
- 11 Y. Gai, J. Li, S.-S. Li, J.-B. Xia and S.-H. Wei, *Phys. Rev. Lett.*, 2009, **102**, 036402.
- 12 S. Zhang, F. Peng, H. Wang, H. Yu, S. Zhang, J. Yang and H. Zhao, *Catal. Commun.*, 2011, **12**, 689–693.
- 13 A. Pandikumar, K. Sivaranjani, C. S. Gopinath and R. Ramaraj, *RSC Adv.*, 2013, **3**, 13390–13398.
- 14 Y. Gao, P. Fang, F. Chen, Y. Liu, Z. Liu, D. Wang and Y. Dai, *Appl. Surf. Sci.*, 2013, **265**, 796–801.
- 15 L. H. Huang, C. Sun and Y. L. Liu, *Appl. Surf. Sci.*, 2007, **253**, 7029–7035.
- 16 S. P. Lim, N. M. Huang, H. N. Lim and M. Mazhar, *Int. J. Photoenergy*, 2014, **2014**, 12.
- 17 C. Su, L. Liu, M. Zhang, Y. Zhang and C. Shao, *CrystEngComm*, 2012, **14**, 3989–3999.
- 18 S. P. Lim, A. Pandikumar, N. M. Huang and H. N. Lim, *RSC Adv.*, 2014, **4**, 38111–38118.
- 19 S. P. Lim, A. Pandikumar, N. M. Huang and H. N. Lim, *Int. J. Hydrogen Energy*, 2014, **39**, 14720–14729.
- 20 G. L. Chiarello, M. H. Aguirre and E. Selli, *J. Catal.*, 2010, **273**, 182–190.
- 21 K. Sivaranjani and C. S. Gopinath, *J. Mater. Chem.*, 2011, **21**, 2639–2647.
- 22 T. Ohsaka, F. Izumi and Y. Fujiki, *J. Raman Spectrosc.*, 1978, **7**, 321–324.
- 23 S. Linic, P. Christopher and D. B. Ingram, *Nat. Mater.*, 2011, **10**, 911–921.
- 24 J. Lu, F. Su, Z. Huang, C. Zhang, Y. Liu, X. Ma and J. Gong, *RSC Adv.*, 2013, **3**, 720–724.
- 25 J. Du, J. Zhang, Z. Liu, B. Han, T. Jiang and Y. Huang, *Langmuir*, 2006, **22**, 1307–1312.
- 26 V. Subramanian, E. E. Wolf and P. V. Kamat, *J. Phys. Chem. B*, 2003, **107**, 7479–7485.
- 27 K. Yu, Y. Tian and T. Tatsuma, *Phys. Chem. Chem. Phys.*, 2006, **8**, 5417–5420.
- 28 N. Chandrasekharan and P. V. Kamat, *J. Phys. Chem. B*, 2000, **104**, 10851–10857.
- 29 V. Subramanian, E. E. Wolf and P. V. Kamat, *Langmuir*, 2003, **19**, 469–474.
- 30 H. Wang, S. L. Leonard and Y. H. Hu, *Ind. Eng. Chem. Res.*, 2012, **51**, 10613–10620.
- 31 S. G. Kim, M. J. Ju, I. T. Choi, W. S. Choi, H.-J. Choi, J.-B. Baek and H. K. Kim, *RSC Adv.*, 2013, **3**, 16380–16386.
- 32 P. S. Archana, A. Gupta, M. M. Yusoff and R. Jose, *Phys. Chem. Chem. Phys.*, 2014, **16**, 7448–7454.
- 33 J. Nissfolk, K. Fredin, A. Hagfeldt and G. Boschloo, *J. Phys. Chem. B*, 2006, **110**, 17715–17718.
- 34 Q. Wang, Z. Zhang, S. M. Zakeeruddin and M. Grätzel, *J. Phys. Chem. C*, 2008, **112**, 7084–7092.
- 35 J. M. Kroon, N. J. Bakker, H. J. P. Smit, P. Liska, K. R. Thampi, P. Wang, S. M. Zakeeruddin, M. Grätzel, A. Hinsch, S. Hore, U. Wurfel, R. Sastrawan, J. R. Durrant, E. Palomares, H. Pettersson, T. Gruszecki, J. Walter, K. Skupien and G. E. Tulloch, *Prog. Photovoltaics*, 2007, **15**, 1–18.
- 36 S. Lin, K. Lee, J. Wu and J. Wu, *Sol. Energy*, 2012, **86**, 2600–2605.
- 37 M. Ni, M. K. H. Leung, D. Y. C. Leung and K. Sumathy, *Renew. Sust. Energ. Rev.*, 2007, **11**, 401–425.
- 38 P. Christopher, D. B. Ingram and S. Linic, *J. Phys. Chem. C*, 2010, **114**, 9173–9177.
- 39 S. Pany, K. M. Parida and B. Naik, *RSC Adv.*, 2013, **3**, 4976–4984.
- 40 B. Naik, K. M. Parida and C. S. Gopinath, *J. Phys. Chem. C*, 2010, **114**, 19473–19482.

